

# On the use of far-infrared and sub-millimeter line ratios to constrain the physical properties of gas in high- $z$ galaxies

A. Schimek<sup>1</sup>, C. Ciccone<sup>1</sup>, S. Shen<sup>1</sup>, D. Decataldo<sup>1</sup>, P. Klaassen<sup>2</sup>, and L. Mayer<sup>3</sup>

<sup>1</sup> Institute of Theoretical Astrophysics, University of Oslo, PO Box 1029, Blindern 0315, Oslo, Norway  
e-mail: [alice.schimek@astro.uio.no](mailto:alice.schimek@astro.uio.no)

<sup>2</sup> UK Astronomy Technology Centre, Royal Observatory Edinburgh, Blackford Hill, Edinburgh United Kingdom

<sup>3</sup> Department of Astrophysics, University of Zurich, Winterthurerstrasse 190, CH-8057 Zurich, Switzerland

Received ; accepted

## ABSTRACT

Optical emission line diagnostics, which are a common tool to constrain the properties of the interstellar medium (ISM) of galaxies, become progressively inaccessible at higher redshifts for ground-based facilities. Far-infrared (FIR) emission lines, which are redshifted into atmospheric windows accessible by ground-based sub-millimeter facilities, could provide alternative ISM diagnostics to optical emission lines. We investigate FIR line ratios involving [CII]  $\lambda 158\mu\text{m}$ , [OIII]  $\lambda 88\mu\text{m}$ , [OIII]  $\lambda 52\mu\text{m}$ , [NII]  $\lambda 122\mu\text{m}$  and [NIII]  $\lambda 57\mu\text{m}$ , using synthetic emission lines applied to a high-resolution ( $m_{\text{gas}} = 883.4 M_{\odot}$ ) cosmological zoom-in simulation, including radiative-transfer post processing with KRAMSES-RT at  $z = 6.5$ . We find that the [CII]/[NII]122 ratio is sensitive to the temperature and density of photo-dissociation regions, and thus could be a useful tool to trace the properties of this gas phase in galaxies. We also find that [NII]/[NIII] is a good tracer of the temperature and [OIII]52/[OIII]88 a good tracer of the gas density of HII regions. Emission line ratios containing the [OIII]  $\lambda 88\mu\text{m}$  line are sensitive to high velocity outflowing gas.

**Key words.** Galaxies: halos – Submillimeter: galaxies – Galaxies: high-redshift – Galaxies: ISM – Methods: numerical

## 1. Introduction

Far-infrared (FIR) emission lines are useful tools for the investigation of the interstellar medium (ISM) of galaxies, as they are mostly unaffected by dust extinction (Brauer et al. 2008). In recent years, FIR emission lines have been used to explore the gas properties of galaxies such as ionisation parameter, gas density, gas metallicity, gas temperature and the radiation field (Nagao et al. 2011, 2013; Cormier et al. 2015; Pereira-Santaella et al. 2017; Rigopoulou et al. 2018; Killi et al. 2023; Ramos Padilla et al. 2023; Kumari et al. 2024). At  $z > 2$  several FIR lines are shifted into the sub-millimeter (sub-mm) atmospheric windows, where they can be observed by sensitive ground-based sub-mm telescopes, which makes them attractive tools to characterise the ISM of high-redshift galaxies in the early stages of their evolution.

In Schimek et al. (2024) we presented a line modelling effort including the [CII]  $\lambda 157\mu\text{m}$ , [CI](1-0)  $\lambda 609\mu\text{m}$ , [CI](2-1)  $\lambda 370\mu\text{m}$ , CO(3-2)  $\lambda 866\mu\text{m}$ , and [OIII]  $\lambda 88\mu\text{m}$  lines. In this follow-up work, we adopt the same simulation and fiducial radiative transfer (RT) model as Schimek et al. (2024), and expand it to include the additional transitions of [OIII]  $\lambda 52\mu\text{m}$ , [NII]  $\lambda 122\mu\text{m}$  and [NIII]  $\lambda 57\mu\text{m}$ , which trace the warm gas found in HII regions (Nagao et al. 2011). While in Schimek et al. (2024) the main subject was to study the extended sub-mm emission of the circum-galactic medium (CGM), we now focus on the inner part of the simulation. Inspired by analytical modelling of these line ratios as seen in Nagao et al. (2011) and Pereira-Santaella et al. (2017), we focus on studying how FIR emission line ratios change as functions of ISM properties when applied to a full galaxy simulation. Examples of previously explored FIR emission line ratios are the [OIII]  $\lambda 88\mu\text{m}$  / [CII]  $\lambda 158\mu\text{m}$  ra-

tio, which has been investigated in both local and high-redshift galaxies (Vallini et al. 2015; Inoue et al. 2016; Carniani et al. 2018; Hashimoto et al. 2019; Pallottini et al. 2017, 2019; Katz et al. 2019; Harikane et al. 2020; Arata et al. 2020; Carniani et al. 2020; Lupi et al. 2020; Vallini et al. 2021; Fujimoto et al. 2024; Katz et al. 2022; Pallottini et al. 2022; Witstok et al. 2022; Kumari et al. 2024), and [OIII]  $\lambda 52\mu\text{m}$  / [OIII]  $\lambda 88\mu\text{m}$ , which has been shown to trace the gas density of ionised gas (Dinerstein et al. 1985; Rubin et al. 1994; Brauer et al. 2008; Nagao et al. 2011, 2013; Pereira-Santaella et al. 2017; Rigopoulou et al. 2018; Killi et al. 2023). Our results are aimed to inform observations performed with current and future sub-millimeter facilities such as the Atacama Large Millimeter/submillimeter Array (ALMA), the Atacama Pathfinder Experiment (APEX), the Northern Extended Millimeter Array (NOEMA) and, in the future, the Atacama Large Aperture Submillimetre Telescope (ATLAST)<sup>1</sup> (Mroczkowski et al. 2024).

## 2. Simulation and modelling

In this study we analyse the Ponos simulation (Fiacconi et al. 2017), a high resolution cosmological zoom-in simulation, run with the smoothed particle hydrodynamics (SPH) code GASOLINE (Wadsley et al. 2004). The simulation has a gas mass resolution of  $m_{\text{gas}} = 883.4 M_{\odot}$ , a stellar particle mass of  $m_{\star} = 0.4 \cdot m_{\text{gas}} = 353.4 M_{\odot}$ , and uses WMAP 7/9 cosmology ( $\Omega_{m,0} = 0.272$ ,  $\Omega_{\Lambda,0} = 0.728$ ,  $\Omega_{b,0} = 0.0455$ ,  $\sigma_8 = 0.807$ ,  $n_s = 0.961$ , and  $H_0 = 70.2 \text{ km s}^{-1} \text{ Mpc}^{-1}$ ) (Komatsu et al. 2011; Hinshaw et al. 2013). Ponos is the progenitor of a massive galaxy, undergoing a merger (stellar mass merger ratio 1 : 2.7) in the analysed

<sup>1</sup> <https://www.atlast.uio.no>

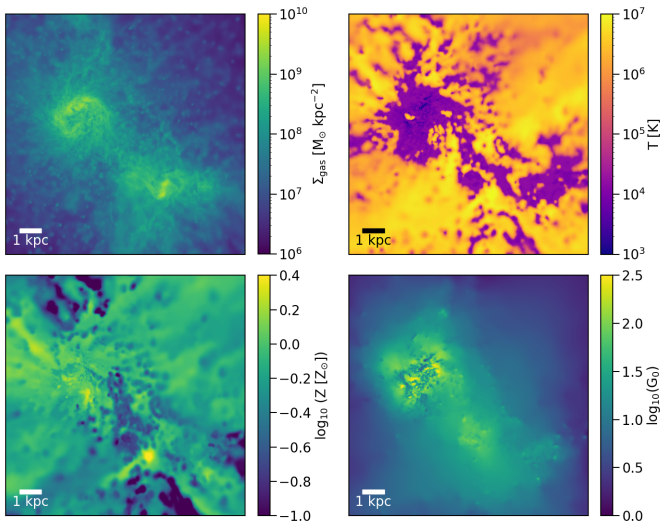


**Fig. 1.** Zoomed-in view of Ponos, focusing on the main disc and the main merger. In the top row the gas surface density is shown on the left, and the gas temperature on the right; in the bottom row the gas phase metallicity is shown on the left, and the FUV field on the right. For full sized images of the simulation see Fig. 1 in Schimek et al. (2024)

snapshot at  $z = 6.5$ . The central galaxy has a stellar mass of  $M_* = 2 \cdot 10^9 M_\odot$ , a virial radius of  $R_{\text{vir}} = 21.18$  kpc, and a star formation rate  $\text{SFR} = 20 M_* \text{ yr}^{-1}$ . These properties make Ponos a typical star forming galaxy at  $z = 6.5$ . Fig. 1 shows the gas density, temperature, metallicity and far-ultraviolet (FUV) radiation field of the main disc and the main merger of Ponos. Figures showing the entire halo can be seen in Schimek et al. (2024).

We refer to Schimek et al. (2024) for the details of emission-line modelling, but briefly outline our fiducial model here. We first converted the Ponos simulation into an adaptive mesh refinement (AMR) grid, and then post-processed it with KRAMSES-RT (Pallottini et al. 2019; Decataldo et al. 2019, 2020), a customised version of RAMSES-RT (Teyssier 2002; Rosdahl et al. 2013) where a non-equilibrium chemical network generated via the package KROME (Grassi et al. 2014) has been implemented. We used the KRAMSES-RT accurate scheme for radiative transport, accounting for photo-reactions and gas self-shielding to compute the radiation in 10 bins for each grid cell. We computed stellar spectra for each star particle with STARBURST 99 (SB99) (Leitherer et al. 1999), according to the age and the metallicity of the stellar particle, and then rescaled it to its mass. In addition to stellar radiation, we included a uniform ultraviolet background (UVB) (Haardt & Madau 2012 tables at  $z = 6.49$ ) and attenuated it in each cell according to the column density of each chemical species. The simulation was further post-processed with CLOUDY (Ferland et al. 2017), creating a multi-dimensional grid for the line emission, based on the gas temperature, gas density, gas metallicity and the incident FUV radiation field. We include the radiation field of the gas with  $G_0$ , which corresponds to the ionising FUV radiation field (6 - 13.6 eV) in units of Habing ( $1.6 \cdot 10^{-3} \text{ erg cm}^{-2} \text{ s}^{-1}$ ) (Habing 1968).

To compute line luminosity ratios and line ratio maps from the post-processed simulation data, we applied a luminosity thresholds of  $L_{\text{line}} > 0.5 L_\odot$  per fluid element, and  $\Sigma_{\text{line}} > 5 L_\odot \text{ kpc}^{-2}$  for the surface luminosity maps to both lines involved in the ratio. These thresholds are very low, and thus do not affect the integrated ratio values of the halo. The integrated line ratios for the entire halo and the different components can be seen

**Table 1.** Integrated line ratio values of Ponos, for the different galaxy components.

Line ratio	Total	Disc	Merger	CGM
$L_{[\text{OIII}]88}/L_{[\text{CII}]158}$	0.17	0.13	0.18	0.39
$L_{[\text{OIII}]52}/L_{[\text{OIII}]88}$	0.36	0.43	0.45	0.13
$L_{[\text{NII}]122}/L_{[\text{NIII}]57}$	1.37	1.36	1.29	1.73
$L_{[\text{CII}]158}/L_{[\text{NII}]122}$	16.92	18.62	14.56	15.15
$L_{[\text{OIII}]88}/L_{[\text{NIII}]57}$	4.01	3.40	3.39	10.28

in Table 1. We follow the same criteria to define the individual galaxy components as in Schimek et al. (2024), but in this study we focus on the disc and merger components within the central 25 kpc, since most lines are faint in the CGM. Due to the applied threshold, most of the far CGM is not included, as the CGM components that are bright enough to satisfy the criteria are located close to the main disc and merger components within the central 25 kpc. We classify the gas as ‘inflows’ and ‘outflows’, in the same way it was done in Schimek et al. (2024). We select the ‘high velocity’ gas with an absolute  $v > 200 \text{ km s}^{-1}$  (higher than the rotational velocity of the main disc), and define it as inflowing or outflowing by dividing it into gas that is flowing towards the main disc and away from the main disc.

### 3. Results

Our results are shown in Fig. 2, displaying emission line ratio maps, and Fig. 3, showing the ratios as a function of gas density, temperature, metallicity, incident FUV radiation field and absolute velocities of the gas cells. In the following, we comment on each line ratio separately.

#### 3.1. O3C2

The  $[\text{OIII}] 88\mu\text{m} / [\text{CII}] 158\mu\text{m}$  (O3C2) ratio is of great interest, as the  $[\text{CII}]$  and the  $[\text{OIII}]$  emission lines are bright coolants of the ISM in the FIR, and can be observed with ground-based telescopes from a high-altitude site at  $z \gtrsim 1$  and  $z \gtrsim 3$  respectively.  $[\text{CII}]$  is one of the brightest FIR emission lines in star-forming (SF) galaxies, accounting for up to 0.1 - 1% of the total FIR emission (Stacey et al. 1991), and traces both ionised and neutral gas, due to the low excitation energy of carbon (11.26 eV, lower than hydrogen with 13.6 eV).  $[\text{OIII}]$  has a high ionisation energy of 35 eV, and traces hot and diffuse gas in HII regions and hot outflows. The O3C2 ratio has been investigated in both observational and theoretical studies of high- and low-redshift galaxies (Vallini et al. 2015; Inoue et al. 2016; Carniani et al. 2018; Hashimoto et al. 2019; Pallottini et al. 2017, 2019; Katz et al. 2019; Harikane et al. 2020; Arata et al. 2020; Carniani et al. 2020; Lupi et al. 2020; Vallini et al. 2021; Fujimoto et al. 2024; Katz et al. 2022; Pallottini et al. 2022; Witstok et al. 2022; Kumari et al. 2024; Ramos Padilla et al. 2023). As the  $[\text{CII}]$  and  $[\text{OIII}]88\mu\text{m}$  lines trace different gas phases within the ISM, the analysis of the emission line ratio can give information about the physical conditions of the ISM, such as the PDR covering fraction, gas densities and temperatures.

In Schimek et al. (2024) we showed that  $[\text{CII}]$  emission is more extended than  $[\text{OIII}]$ , and while the respective line luminosities fall within the scatter of observational data, Ponos (total O3C2 ratio of 0.17) is more aligned with ratios in the local universe than with high-redshift galaxies which have observed ratios between 1 - 10 (Harikane et al. 2020). We note that local dwarf galaxies, often used as analogues of early galaxies, ap-

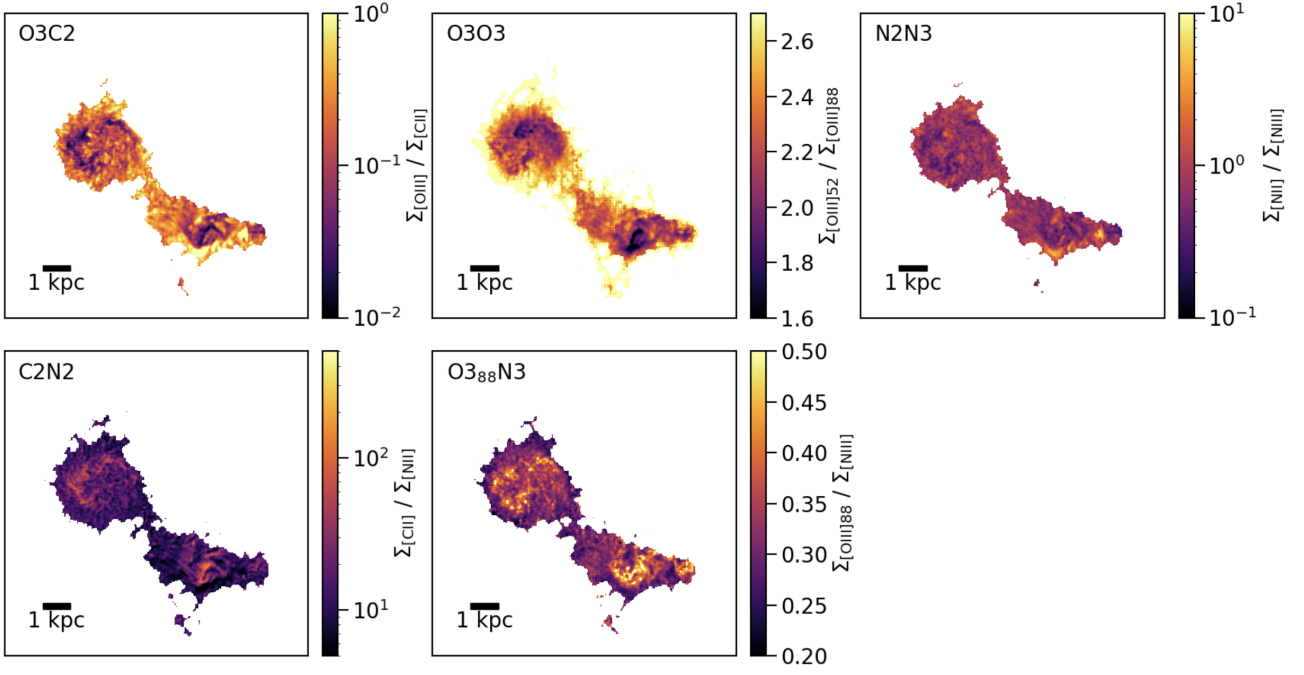


**Fig. 2.** Line ratio maps resulting from our modelling. Because of the surface brightness cuts applied to both lines involved in the ratios ( $\Sigma_{\text{line}} > 5 L_{\odot} \text{ kpc}^{-2}$ ) only the central disc, major merger, and inner CGM components are probed. Only the central 25 kpc of the Ponos simulation halo is shown.

pear to share some of these extreme conditions, with [CII] being more extended than [OIII] (Cormier et al. 2015) and O3C2 ratios exceeding unity (Kumari et al. 2024). One of the reasons for the enhanced ratios measured at high-redshift could lie in abundance ratio differences due to an early stage of chemical evolution (see Nyhagen et al. in prep). The O3C2 map, reported in the upper left panel of Fig. 2, shows that the ratio is significantly enhanced in spatially compact areas in the disc, which correspond to hot, low density and high metallicity regions (see Fig. 1).

In Fig. 3, where the first row corresponds to the O3C2 ratio, we find that the O3C2 ratio is most sensitive to both gas density and temperature, as it varies by four orders of magnitude, being low in high density ( $n \sim 10^3 \text{ cm}^{-3}$ ) and low temperature gas ( $T \sim 8 \cdot 10^3 \text{ K}$ ), and high in low density ( $n \sim 5 \cdot 10^{-3} \text{ cm}^{-3}$ ) and high temperature gas ( $T \sim 5 \cdot 10^5 \text{ K}$ ). We find O3C2 ratio values of  $\leq 1$  for typical values of HII regions ( $T \sim 7 \cdot 10^3 - 1.5 \cdot 10^4 \text{ K}$ ,  $n \sim 10 - 10^2 \text{ cm}^{-3}$ , Osterbrock & Ferland (2006)). The highest ratios ( $\geq 10$ ) are found in gas with typical densities and temperatures of SNe remnants ( $T \sim 10^{5.7} \text{ K}$ ,  $n \sim 10^{-2.5} \text{ cm}^{-3}$ , McKee & Ostriker (1977)). We see a small scatter for the ratio as a function of the density and temperature, and also do not see significant differences between the ISM components of the disc and the merger and the CGM, probably because this analysis, as explained in Section 2, is not sensitive to the most extended CGM gas. The dependence of O3C2 on the radiation field seems not very significant up to  $\log_{10}(G_0) \sim 2$ , above which the ratio increases as the strong radiation can ionise [OIII], while carbon is doubly ionised, decreasing the [CII] emission. As we assume uniform solar abundance ratios for the gas in our CLOUDY modelling, which are scaled with the metallicity, the lack of dependence of the O3C2 ratio on the gas phase metallicity for sub-solar metallicities is not surprising. For all metallicities, the C/O ratio is constant in our models, while in galaxies the C/O ratio would be metallicity dependent due to the different timescales of enrichment processes (Maiolino & Mannucci 2019; Arata et al.

2020). At super-solar metallicities, we see a sharp increase of the O3C2 ratio by two orders of magnitude. We note that only a small fraction of the gas mass in Ponos (5.2%) reaches such high metallicities. The increase of the ratio as a function of metallicity is caused by the properties of the gas, as it seems to have been recently enriched by core-collapse supernova (cc-SNe), and is generally heated, has low densities, and experiences a strong radiation field. At  $\log_{10}(Z/Z_{\odot}) \geq 0.2$  we find gas with  $\text{O3C2} \geq 10$ , with temperatures of  $10^4 - 2 \cdot 10^4 \text{ K}$ , densities of  $n \sim 0.1 - 10 \text{ cm}^{-3}$ . It also experiences strong radiation fields of  $\log(G_0) \sim 2.0 - 2.5$ . We attribute the sharp increase of the O3C2 emission line ratio for super-solar metallicities to the effect of the radiation field, as well as the low gas densities and high temperatures. From observational results (Cormier et al. 2015) and theoretical modelling where individual elements are traces (Arata et al. 2020) we would expect lower O3C2 ratios at higher metallicities. Directly tracing carbon and oxygen with their respective yields caused by different enrichment events (e.g. cc-SNe, SN Type Ia, asymptotic giant branch (AGB) stars, etc.) could reveal a significant metallicity dependence. Arata et al. (2020) found in their semi-analytical modelling that the O3C2 ratio decreases by two orders of magnitude with increasing metallicity, which could counteract the trend we find when assuming a fixed, metallicity independent C/O ratio. The ratio has a larger scatter as a function of both gas phase metallicity and radiation field, compared to density and temperature ( $\leq 0.5$  dex). The last column of Fig. 3 shows the ratio as a function of the absolute velocity of the gas, divided into inflowing and outflowing components. It can be seen that outflowing gas shows higher O3C2 ratios compared to inflowing gas, due to gas heated by SNe feedback, where [OIII] radiation dominates.



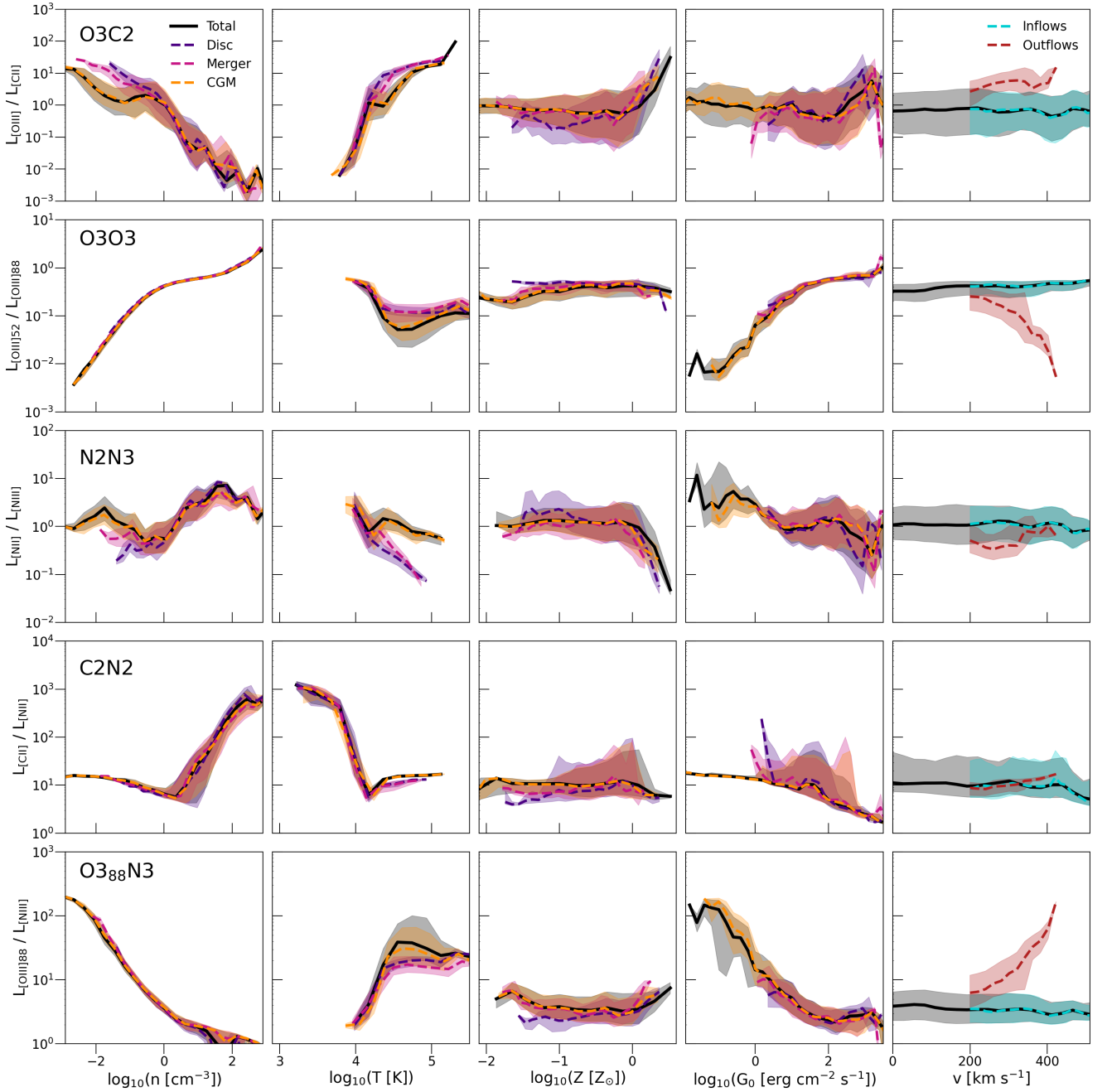


**Fig. 3.** Median of the line ratios plotted as a function of gas density, temperature, metallicity, UV field, and absolute velocity of the gas cells. The ratios are divided into the total halo (black), the disc (indigo), the merger components (magenta) and the CGM (orange), except for the absolute velocity panel, where we divide the gas into inflowing (blue) and outflowing (red) gas. The shaded areas correspond to the 25th and 75th percentiles.

### 3.2. $O_{352}O_{388}$

The  $[OIII] \lambda 52\mu m / [OIII] \lambda 88\mu m$  ( $O_{352}O_{388}$ ) ratio has been found to be an indicator for the gas density (Dinerstein et al. 1985; Rubin et al. 1994; Brauher et al. 2008; Nagao et al. 2011, 2013; Pereira-Santaella et al. 2017; Rigopoulou et al. 2018; Killi et al. 2023; Nakazato et al. 2023). Indeed, in contrast to the optical  $[OIII]$  lines (e.g. 4363Å, 4959Å, 5007Å), the FIR  $[OIII]$  line ratio is less dependent on the electron temperature and more sensitive to the electron density (Dinerstein et al. 1985).

The total  $O_{352}O_{388}$  of Ponos is 0.36. Recent ALMA observations by Killi et al. (2023) found a ratio of 0.7 for a galaxy at  $z = 7$ , which is a factor of two higher than Ponos. Simula-

tion work by Nakazato et al. (2023) found their simulated galaxies at  $z = 7$  to have ratios  $\leq 1$ , ranging from about 0.8 - 1.0. Our result, as well as the findings by Killi et al. (2023) and Nakazato et al. (2023) are lower than local galaxies (Brauher et al. 2008), and local planetary nebulae (Dinerstein et al. 1985). As shown in the second panel of Fig. 2, there are spatial variations in the map, with generally lower ratios in the inner regions of the disc and merger, which radially increase towards the outskirts. In the second row of Fig. 3, the strongest dependency can be seen on the gas density, where the scatter is also very small, which is in agreement with previous findings (Nagao et al. 2011; Pereira-Santaella et al. 2017). This is because the two  $[OIII]$  lines have slightly different critical densities ( $3.6 \cdot 10^3 \text{ cm}^{-3}$

for [OIII]52 and  $5.1 \cdot 10^2 \text{ cm}^{-3}$  for [OIII]88 respectively) and thus their ratio is sensitive to the gas density. Higher densities lead to higher ratios, with an increase of four orders of magnitude from  $n = 10^{-2.5} \text{ cm}^{-3}$  to  $n = 10^{2.5} \text{ cm}^{-3}$ . The dependency on temperature is weak and degenerate, as higher O<sub>3</sub>2O<sub>3</sub>88 ratio values are associated with both low and high temperatures. All galaxy components show a completely flat trend of O<sub>3</sub>2O<sub>3</sub>88 as a function of gas metallicity, which is expected as both lines trace the same element. There is a dependency on the radiation field, where we see a rise in ratio towards higher radiation fields. The outflowing and inflowing component show a significant difference in ratio as a function of the velocity, where the ratio of the outflowing gas decreases by over an order of magnitudes. This indicates that the [OIII]88 line is a stronger tracer of outflows than the [OIII]52 emission line.

### 3.3. N2N3

The [NII]  $\lambda 122\mu\text{m}$  / [NIII]  $\lambda 57\mu\text{m}$  (N2N3) ratio can be used to study the ionisation parameter of the gas (Nagao et al. 2011), and to measure the effective temperature of stars ionising the gas (Rubin et al. 1994; Brauer et al. 2008). Singularity ionised nitrogen (N<sup>+</sup>) has an ionisation potential of 14.53 eV, and a critical density of  $3.1 \cdot 10^2 \text{ cm}^{-3}$ , and thus [NII] traces lower temperature areas in ionised HII regions than doubly ionised nitrogen (N<sup>++</sup>), which has an ionisation potential of 29.60 eV.

From the third panel of Fig. 2, it can be seen that, in contrast to the previously discussed ratios, the N2N3 ratio is almost uniform across the source, with an enhancement in small areas of lower temperature ionised gas ( $10^4 \text{ K} < T < 10^{4.5} \text{ K}$ ), where [NII] dominates. In the third row of Fig. 3, we see that the N2N3 ratio is degenerate with gas density. The most significant dependency of this ratio is on the gas temperature, where we see higher temperatures leading to lower ratios. The decrease of N2N3 as a function of temperature is steeper for disc and merger components than for the CGM, because of the low radiation field strength of the CGM. As metals in gas promote the cooling, we investigated if the ability of nitrogen to trace the temperature of the ionised gas could be affected by a change in metallicity. We found no significant differences in the dependency of the N2N3 ratio on the temperature at different metallicities.

The N2N3 ratio does not depend on the metallicity, until we reach super-solar values, where the ratio rapidly drops, which can once again be connected to hot gas that has been enriched by SNe, and experiences a strong radiation field, which is the same trend we see in the corresponding increase of O3C2. There is also a dependency on the radiation field, with higher ratios for lower radiation fields, which is caused by the lower ionisation energy of [NII] compared to [NIII]. We do not detect a significant difference in N2N3 ratio between inflows and outflows. Due to the weak dependencies on density and metallicity, we find that N2N3 can be used as a diagnostic tool to constrain the ionised gas temperature. We also find a dependency on the radiation field, and thus the ionisation of the gas, which is in agreement with Nagao et al. (2011), who found that N2N3 traces the ionisation parameter.

### 3.4. C2N2

Like the O3C2 ratio, the [CII]  $\lambda 158\mu\text{m}$  / [NII]  $\lambda 122\mu\text{m}$  (C2N2) ratio uses two emission lines that originate from different phases of the ISM. The [CII] and [NII] lines have ionisation energies of 11.26 eV and 14.53 eV respectively, which are both close to

the ionisation energy of hydrogen (13.6 eV). Previous studies have tested the [CII]  $\lambda 158\mu\text{m}$  / [NII]  $\lambda 205\mu\text{m}$  (or [NII]205/[CII]) ratio, and proposed it to be a tracer of metallicity (Nagao et al. 2013), and as a tracer to constrain the fraction of [CII] emission that is associated with ionised gas (Decarli et al. 2014) and to scale with the IR-luminosity (Cunningham et al. 2020). The ratio of [CII] and [NII]122 has not yet been well explored.

The spatially resolved map of this ratio (bottom-left panel of Fig. 2) shows higher values in dense structures of the disc. The plots reported in Fig. 3 (fourth row) shows evidence for a phase transition of C2N2 as a function of density and temperature. In the low density regime, the ratio has a slight tendency to decrease with increasing density until it reaches a turning point at  $n = 5 \text{ cm}^{-3}$ , above which the ratio rapidly increases by two orders of magnitude with density. [CII] has a wide range of critical densities for collisions with electrons, atoms or molecules ( $5 \text{ cm}^{-3}$  up to  $10^3 \text{ cm}^{-3}$ ), and the C2N2 ratio starts to increase when the minimum critical density is reached. The same behaviour can be seen in the temperature, where the ratio quickly drops off by two orders of magnitude until it reaches a temperature slightly above  $10^4 \text{ K}$ , after which it remains roughly constant with temperature. Therefore, denser and colder regions of the ISM are more sensitive to the C2N2 ratio than diffuse gas, which can also be seen in the map from Fig. 2. The turning point in both temperature and density shows evidence for a phase transition from ionised HII regions, to neutral PDR regions. Therefore we find that the C2N2 ratio could be used to infer the gas density and temperature of PDR regions, as it seems to be most sensitive in this regime. On the other hand, the C2N2 ratio is insensitive to the gas phase metallicity. This insensitivity would not significantly change if we would directly trace the abundances of elements, as the C/N ratio has been found to be approximately constant over a wide range of metallicities (Garnett et al. 1999; Berg et al. 2016; Pereira-Santaella et al. 2017). The ratio is also only slightly sensitive to the radiation field, where a large scatter within the disc component can be seen. In the merger and the disc the ratio increases towards lower radiation fields, which corresponds to shielded, denser gas. There is a general weak trend for lower ratios at higher radiation fields. We see no differences in C2N2 ratio between the outflowing and the inflowing gas.

### 3.5. O3N3

The [OIII]  $\lambda 88\mu\text{m}$  / [NIII]  $\lambda 57\mu\text{m}$  (O3N3) ratio is a candidate for tracing the gas metallicity, as it is a good proxy for the N/O abundance ratio (Nagao et al. 2011; Pereira-Santaella et al. 2017). Both lines have similar ionisation energies, and thus trace the same gas in HII regions, which is important for metallicity calibrations (Méndez-Delgado et al. 2023). To account for the dependence of the [OIII] lines on the electron density of the gas, the O3N3 ratio often combines the [OIII]88 and the [OIII]52 line (Pereira-Santaella et al. 2017). In our analysis we found that including the [OIII]52 line does not change our results, and thus we focus on the ratio including only the [OIII]88 line (which is easier to observe from ground). As discussed above for the O3C2 ratio, the assumption of constant abundance ratios in our modelling limits our capability of exploring true metallicity dependencies.

The second panel of the second row of Fig. 2 shows the O3N3 ratio map. As both lines originate from similar phases of the gas, the spatial variation of the ratio is small. The O3N3 ratio is higher in the inner regions of the disc, with small areas with highly increased ratios within the ISM, which correspond to hot and diffuse regions like HII regions and SNe sites, where

[OIII] dominates. In the bottom row of Fig. 3 we can see a strong dependency of the ratio on the gas density, whereby the ratio decreases by over two orders of magnitude within the explored density range. The trend with the temperatures shows a similar behaviour, where gas with lower temperatures also has a lower ratio, and flattening towards higher temperatures. The radiation field seems to be the strongest dependency we find, where high radiation fields lead to a low ratio, rising by two orders of magnitude. Interestingly, we see a significant difference in ratio between outflowing and inflowing gas, whereby for the former, the O3N2 ratio increases by an order of magnitude as a function of velocity.

#### 4. Conclusions

In this work we investigated FIR emission line ratios in the context of a cosmological zoom-in simulation of a high-redshift galaxy, to assess how much these ratios can tell us about the galaxy's ISM properties. Our main results can be summarised as follows:

- We discovered that C2N2 can be used as a tracer to infer the density and temperature of PDR regions;
- O3O3 is confirmed to be a good tracer for the gas phase density, although we also find a dependency on the incident radiation field;
- We find a significant difference of O3C2, O3O3 and O3N3 in in- and outflowing gas, suggesting that these ratios could be used to analyse high velocity components. [OIII]88  $\mu$ m is sensitive to high velocity outflowing gas;
- N2N3 is found to be a good tracer of the temperature of ionised gas and confirmed to trace the radiation field in the ISM of galaxies;

*Acknowledgements.* This project has received funding from the European Union's Horizon 2020 research and innovation program under grant agreement No 951815 (AtLAST). We thank the anonymous referee for providing insightful comments that helped us improve the analysis and interpretation of the results. The simulations were performed using the resources from the National Infrastructure for High Performance Computing and Data Storage in Norway, UNINETT Sigma2, allocated to Project NN9477K. We acknowledge usage of the Python programming language (Van Rossum & Drake Jr 1995; Van Rossum & Drake 2009), Matplotlib (Hunter 2007), NumPy (van der Walt et al. 2011), and Pynbody (Pontzen et al. 2013).

#### References

- Arata, S., Yajima, H., Nagamine, K., Abe, M., & Khochfar, S. 2020, *MNRAS*, 498, 5541
- Berg, D. A., Skillman, E. D., Henry, R. B. C., Erb, D. K., & Carigi, L. 2016, *ApJ*, 827, 126
- Brauer, J. R., Dale, D. A., & Helou, G. 2008, *ApJS*, 178, 280
- Carniani, S., Ferrara, A., Maiolino, R., et al. 2020, *MNRAS*, 499, 5136
- Carniani, S., Maiolino, R., Amorin, R., et al. 2018, *MNRAS*, 478, 1170
- Cormier, D., Madden, S. C., Lebouteiller, V., et al. 2015, *A&A*, 578, A53
- Cunningham, D. J. M., Chapman, S. C., Aravena, M., et al. 2020, *MNRAS*, 494, 4090
- Decarli, R., Walter, F., Carilli, C., et al. 2014, *The Astrophysical Journal Letters*, 782, L17
- Decataldo, D., Lupi, A., Ferrara, A., Pallottini, A., & Fumagalli, M. 2020, *MNRAS*, 497, 4718
- Decataldo, D., Pallottini, A., Ferrara, A., Vallini, L., & Gallerani, S. 2019, *MNRAS*, 487, 3377
- Dinerstein, H. L., Lester, D. F., & Werner, M. W. 1985, *ApJ*, 291, 561
- Ferland, G. J., Chatzikos, M., Guzmán, F., et al. 2017, *Rev. Mexicana Astron. Astrofis.*, 53, 385
- Fiacconi, D., Mayer, L., Madau, P., et al. 2017, *MNRAS*, 467, 4080
- Fujimoto, S., Ouchi, M., Nakajima, K., et al. 2024, *ApJ*, 964, 146
- Garnett, D. R., Shields, G. A., Peimbert, M., et al. 1999, *ApJ*, 513, 168
- Grassi, T., Bovino, S., Schleicher, D. R. G., et al. 2014, *MNRAS*, 439, 2386
- Haardt, F. & Madau, P. 2012, *ApJ*, 746, 125
- Habing, H. J. 1968, *Bull. Astron. Inst. Netherlands*, 19, 421
- Harikane, Y., Ouchi, M., Inoue, A. K., et al. 2020, *ApJ*, 896, 93
- Hashimoto, T., Inoue, A. K., Mawatari, K., et al. 2019, *Publications of the Astronomical Society of Japan*, 71, 71
- Hinshaw, G., Larson, D., Komatsu, E., et al. 2013, *ApJS*, 208, 19
- Hunter, J. D. 2007, *Computing in Science & Engineering*, 9, 90
- Inoue, A. K., Tamura, Y., Matsuo, H., et al. 2016, *Science*, 352, 1559
- Katz, H., Galligan, T. P., Kimm, T., et al. 2019, *MNRAS*, 487, 5902
- Katz, H., Rosdahl, J., Kimm, T., et al. 2022, *MNRAS*, 510, 5603
- Killi, M., Watson, D., Fujimoto, S., et al. 2023, *MNRAS*, 521, 2526
- Komatsu, E., Smith, K. M., Dunkley, J., et al. 2011, *ApJS*, 192, 18
- Kumari, N., Smit, R., Leitherer, C., et al. 2024, *MNRAS*, 529, 781
- Leitherer, C., Schaerer, D., Goldader, J. D., et al. 1999, *ApJS*, 123, 3
- Lupi, A., Pallottini, A., Ferrara, A., et al. 2020, *MNRAS*, 496, 5160
- Maiolino, R. & Mannucci, F. 2019, *A&A Rev.*, 27, 3
- McKee, C. F. & Ostriker, J. P. 1977, *ApJ*, 218, 148
- Méndez-Delgado, J. E., Esteban, C., García-Rojas, J., Kreckel, K., & Peimbert, M. 2023, *Nature*, 618, 249
- Mroczkowski, T., Gallardo, P. A., Timpe, M., et al. 2024, *arXiv e-prints*, arXiv:2402.18645
- Nagao, T., Maiolino, R., De Breuck, C., et al. 2013, in *Astronomical Society of the Pacific Conference Series*, Vol. 476, *New Trends in Radio Astronomy in the ALMA Era: The 30th Anniversary of Nobeyama Radio Observatory*, ed. R. Kawabe, N. Kuno, & S. Yamamoto, 29
- Nagao, T., Maiolino, R., Marconi, A., & Matsuhara, H. 2011, *A&A*, 526, A149
- Nakazato, Y., Yoshida, N., & Ceverino, D. 2023, *ApJ*, 953, 140
- Osterbrock, D. E. & Ferland, G. J. 2006, *Astrophysics of gaseous nebulae and active galactic nuclei* (University Science Books)
- Pallottini, A., Ferrara, A., Bovino, S., et al. 2017, *MNRAS*, 471, 4128
- Pallottini, A., Ferrara, A., Decataldo, D., et al. 2019, *MNRAS*, 487, 1689
- Pallottini, A., Ferrara, A., Gallerani, S., et al. 2022, *MNRAS*, 513, 5621
- Pereira-Santaella, M., Rigopoulou, D., Farrah, D., Lebouteiller, V., & Li, J. 2017, *Monthly Notices of the Royal Astronomical Society*, 470, 1218
- Pontzen, A., Roškar, R., Stinson, G., & Woods, R. 2013, *pynbody: N-Body/SPH analysis for python*
- Ramos Padilla, A. F., Wang, L., van der Tak, F. F. S., & Trager, S. C. 2023, *A&A*, 679, A131
- Rigopoulou, D., Pereira-Santaella, M., Magdis, G. E., et al. 2018, *MNRAS*, 473, 20
- Rosdahl, J., Blaizot, J., Aubert, D., Stranex, T., & Teyssier, R. 2013, *MNRAS*, 436, 2188
- Rubin, R. H., Simpson, J. P., Lord, S. D., et al. 1994, *ApJ*, 420, 772
- Schimek, A., Decataldo, D., Shen, S., et al. 2024, *A&A*, 682, A98
- Stacey, G., Townes, C., Poglitsch, A., et al. 1991, *The Astrophysical Journal*, 382, L37
- Teyssier, R. 2002, *A&A*, 385, 337
- Vallini, L., Ferrara, A., Pallottini, A., Carniani, S., & Gallerani, S. 2021, *MNRAS*, 505, 5543
- Vallini, L., Gallerani, S., Ferrara, A., Pallottini, A., & Yue, B. 2015, *ApJ*, 813, 36
- van der Walt, S., Colbert, S. C., & Varoquaux, G. 2011, *Computing in Science and Engineering*, 13, 22
- Van Rossum, G. & Drake, F. L. 2009, *Python 3 Reference Manual* (Scotts Valley, CA: CreateSpace)
- Van Rossum, G. & Drake Jr, F. L. 1995, *Python reference manual* (Centrum voor Wiskunde en Informatica Amsterdam)
- Wadsley, J. W., Stadel, J., & Quinn, T. 2004, *New A*, 9, 137
- Witstok, J., Smit, R., Maiolino, R., et al. 2022, *MNRAS*, 515, 1751

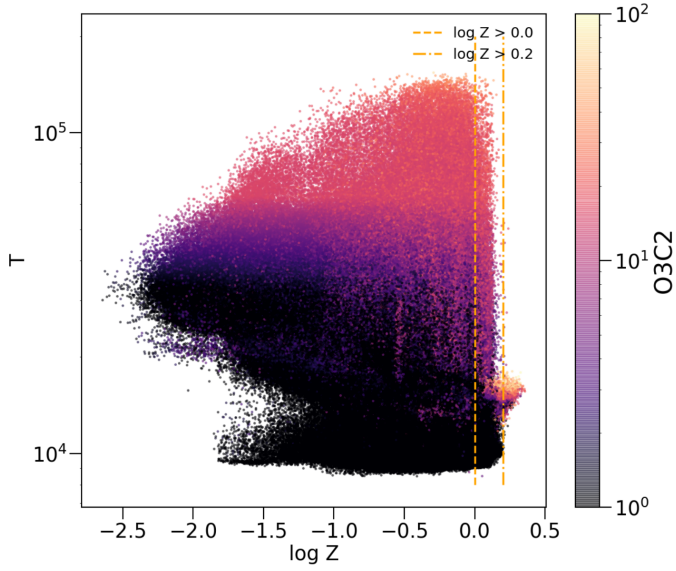


**Fig. A.1.** Phase diagram of gas phase metallicity and gas temperature for gas emitting both in [CII] and [OIII], colour coded by the O3C2 ratio. The vertical dashed line marks solar metallicity, while the dash-dotted line marks  $\log_{10}(Z/Z_{\odot}) = 0.2$ .

## Appendix A: High metallicity gas

As stated in [subsection 3.1](#), we investigate the reason behind the increase of the O3C2 ratio at super-solar metallicities in more detail. [Figure A.1](#) shows the phase diagram of the gas emitting in both [CII] and [OIII], with the metallicity on the x-axis and the temperature on the y-axis. As can be seen there is a wide range of temperatures at high metallicity, reaching above  $10^5$  K. This high temperatures gas also shows high emission line ratios. Additionally, there is a small region within the phase diagram with very high metallicities, that resides within a small temperature range of around  $2 \cdot 10^4$  K, which also displays very high ratios. This gas experiences a high FUV radiation field ( $\log_{10}(G_0) \sim 2 - 2.5$ ) and drives the high metallicity ratio in [Fig. 3](#).

## Appendix B: Metallicity effects on the N2N3 ratio

As metallicity affects the cooling of the gas, it could influence the ability of nitrogen to trace the temperature of the ionised gas. To investigate this in more detail, we divided the gas of the main disc and the merger component into metallicity bins, to study variations of this ratio as a function of temperature for different metallicities. This can be seen in [Fig. B.1](#), where the N2N3 luminosity ratio is plotted as a function of temperature for the different metallicity bins. The plot shows that we see the same steep decreasing trend with temperature for all metallicity bins. We do not see a significant difference in the dependency based on the metallicity of the gas.

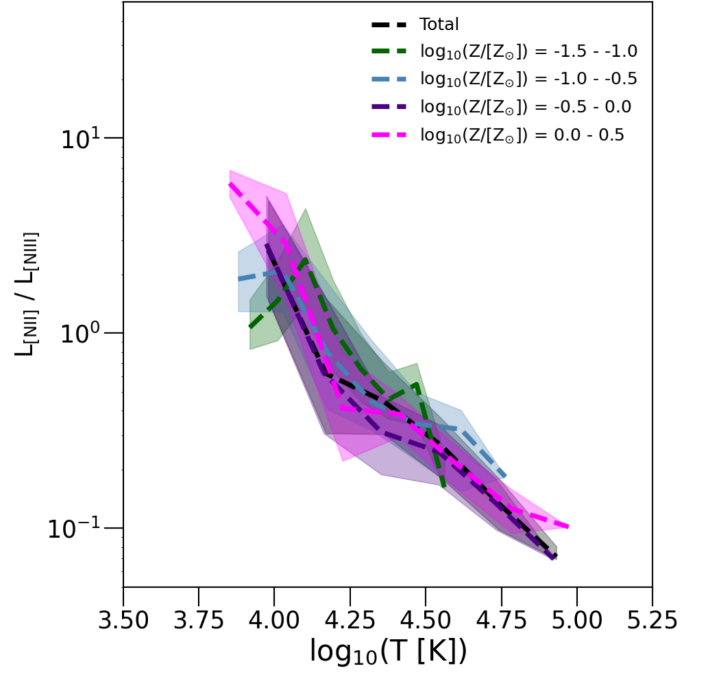


**Fig. B.1.** N2N3 luminosity ratio as a function of temperature, showing the total trend and the gas divided into different metallicity bins.